

# Excitation-assisted nonadiabatic charge-transfer reaction in a mixed atom-ion system

Ming Li,<sup>1</sup> Michael Mills,<sup>2</sup> Prateek Puri,<sup>2</sup> Alexander Petrov,<sup>1,3</sup> Eric R. Hudson,<sup>4</sup> and Svetlana Kotochigova<sup>1</sup>

<sup>1</sup>Department of Physics, Temple University, Philadelphia, PA 19122, USA

<sup>2</sup>Department of Physics and Astronomy, University of California, Los Angeles, California 90095, USA

<sup>3</sup>NRC Kurchatov Institute PNPI, Gatchina, Leningrad district 188300; and Division of Quantum Mechanics, St. Petersburg State University, St. Petersburg, 199034, RF

<sup>4</sup>Department of Physics and Astronomy, University of California, Los Angeles, California 90095, USA

An important physical process unique to neutral-ion systems is the charge-transfer (CT) reaction. Here, we present measurements of and models for CT processes between co-trapped ultracold Ca atoms and Yb ions under well-controlled conditions. The theoretical analysis reveals the existence of three reaction mechanisms when lasers from a magneto-optical trap (MOT) and an additional catalyst laser are present. Besides the direct CT involving existent excited Ca population in the MOT, the second pathway is controlled by MOT-induced CT, whereas the third one mostly involves the additional red-detuned laser.

## I. INTRODUCTION

Over the last few decades the study of individual quantum systems decoupled from external perturbations has become a reality. Combining quantum-degenerate gases of fermionic or bosonic atoms, held in electro-magnetic traps with a wide range of geometries, with cooled and trapped ions is an exciting and dynamic area in physics. Cold and trapped atom-ion mixtures can be engineered with a high level of control, detected state selectively, and even constructed at the single-ion level. The majority of experimental and theoretical research into charge-transfer (CT) with ultracold atoms and ions has focused on their collisions when prepared in their electronic ground state [1–18]. Often, however, cold atom-ion experiments involve holding the neutral atoms in a magneto-optical trap (MOT), providing opportunities for scattering of electronically-excited atoms with the co-trapped ions. Although the first steps towards understanding these collisions have been reported [9, 19, 20], theoretical details are still poorly understood.

Charge-transfer can only be realized through transitions between two or more potential energy surfaces (PESs) that are characterized by electron transfer from the neutral atom to the ion, i.e.  $A^+ + B \rightarrow A + B^+$ . In the conventional Born-Oppenheimer (BO) adiabatic picture, such transitions occur due to non-adiabatic coupling induced by the nuclear motion in the initial and final electronic states [21]. Usually, this coupling occurs in a small localized range of inter-particle separations  $R$ , when electronic BO potentials of the same symmetry have a so-called avoided crossing following the Wigner-Witmer non-crossing rule.

When an avoided crossing between entrance and exit BO potentials is broad like the cases for many heteronuclear atom-ion pairs in their electronic ground states, the charge-transfer rate coefficients are very small, in most cases of the order on  $10^{-14}$  cm<sup>3</sup>/s or below [7, 18, 22, 23]. On the other hand, in a region where molecular structure is complex and potential curves are dense, there is large probability of having narrower avoided crossings

that will lead to much higher charge-transfer rate coefficients, sometimes approaching values of universal models [20, 24]. Our study provides clear evidence of such a situation when a number of closely lying excited potentials, populated through excitation laser, couple strongly via non-adiabatic couplings leading to significant charge-transfer reactions. Even though the atoms in the MOT spend most of their time in the ground electronic state, the rate coefficients can still reach four orders of magnitude higher than that of pure ground-state CT reactions.

Here, we study collisions between Ca atoms in a MOT and Yb<sup>+</sup> ions in a co-located linear-quadrupole ion trap. In this system, CT reactions involve excited 4s4p <sup>1</sup>P Ca atoms and ground-state Yb<sup>+</sup> ions. Experimental and theoretical CT rate coefficients are obtained and compared for temperatures  $0.01 \text{ K} < T < 1 \text{ K}$ . Theoretically, we use hybrid quantum simulations based on ground- and excited-state molecular potentials that combine quantum close-coupling calculations with rate equations for populations. Special attention has been given to the long-range induction and dispersion interactions within the molecular complex as the dissociation limits of excited-state potentials are in proximity and non-adiabatic transfer between the potentials occurs at relatively large separations. We incorporate spontaneous emission from excited-state potentials and include survival probabilities as an important element in our model. To further elucidate the role of excited states in CT an additional catalyst laser with a frequency that is red detuned from that of the MOT laser is applied. As we will show, the effect of spontaneous emission on the reaction path is then suppressed.

We will show that up to three mechanisms or pathways contribute to the reaction outcome. Only the third pathway involves the additional catalyst laser. In the first, an atom in the excited state collides and reacts with the ion. In the second, a ground-state atom in the presence of the long-range interaction from a ground-state ion is resonantly excited by absorption of a photon from the MOT lasers and then reacts with the ion. Finally, for the third pathway a colliding ground-state atom-ion pair absorbs a photon from the tunable catalyst laser and then reacts.

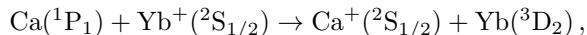
In all pathways the long-range interaction potentials between the cold atom and ion together with spontaneous emission from the electronically-excited atom-ion complex determine the rate coefficients.

## II. MODELING CHARGE-TRANSFER PATHWAYS

### A. Molecular complex and pathways

We start our analysis with the potential energy landscape for the excited-state CT reaction. Figure 1(a) shows the relevant long-range diabatic  $|\Omega| = 1/2, 3/2$  and  $5/2$  potentials, derived from the multipole expansion of the molecular forces, dissociating to the  $\text{Ca}(4s4p\ ^1P_1)+\text{Yb}^+(6s\ ^2S)$  limit as well as to the nearly-degenerate  $\text{Ca}^+(4s\ ^2S)+\text{Yb}(5d6s\ ^3D_2)$  limit. Their asymptotic splitting is only  $\Delta = hc \times 37.7\ \text{cm}^{-1}$ , where  $h$  is the Planck constant and  $c$  is the speed of light in vacuum. Moreover, the molecular electronic state of each diabatic potential is a unique element of the separation-independent ‘‘atomic basis’’ of products of the relevant atomic or ionic Ca and Yb states. The projection of the total electron angular momentum on the internuclear axis,  $\Omega$ , is a good quantum number. Charge-transfer only occurs between states with the same  $\Omega$ , which for our system occurs for  $|\Omega| = 1/2$  potentials near the two crossings at  $R \approx 40a_0$ , where  $a_0$  is the Bohr radius. Spin-orbit couplings are included which are essential for the exit channels dissociating to the  $\text{Ca}^+(4s\ ^2S)+\text{Yb}(5d6s\ ^3D_2)$  limit. Details of our calculation of the potentials and, in particular, the evaluation of the strength of the coupling near the crossing points can be found below as well as in Appendix A.

In a MOT, Ca is present in both its ground  $4s^2\ ^1S_0$  and excited  $4s4p\ ^1P_1$  state. We then define charge-transfer pathway I as



where the initial state is indicated by the arrow in Fig. 1(a) and pathway II as



This second pathway is assisted or dressed by a MOT photon with energy  $\hbar\omega_{\text{MOT}}$  and the  $|\Omega| = 1/2$   $\text{Ca}(4s4p\ ^1P_1)+\text{Yb}^+(6s\ ^2S_{1/2})$  potential is populated as an intermediate state, which then has CT to  $\text{Ca}^++\text{Yb}$  as in the first pathway. Here,  $\hbar$  is the reduced Planck constant. The MOT photon is detuned one natural linewidth,  $\Gamma$ , to the red of the  $\text{Ca}\ ^1S_0 \rightarrow ^1P_1$  transition leading to an avoided crossing at separations of more than a thousand Bohr radii. The repulsive excited  $|\Omega| = 1/2$  and  $3/2$  channels are also populated due to the laser coupling, but do not lead to significant CT reaction.

The third (III) pathway

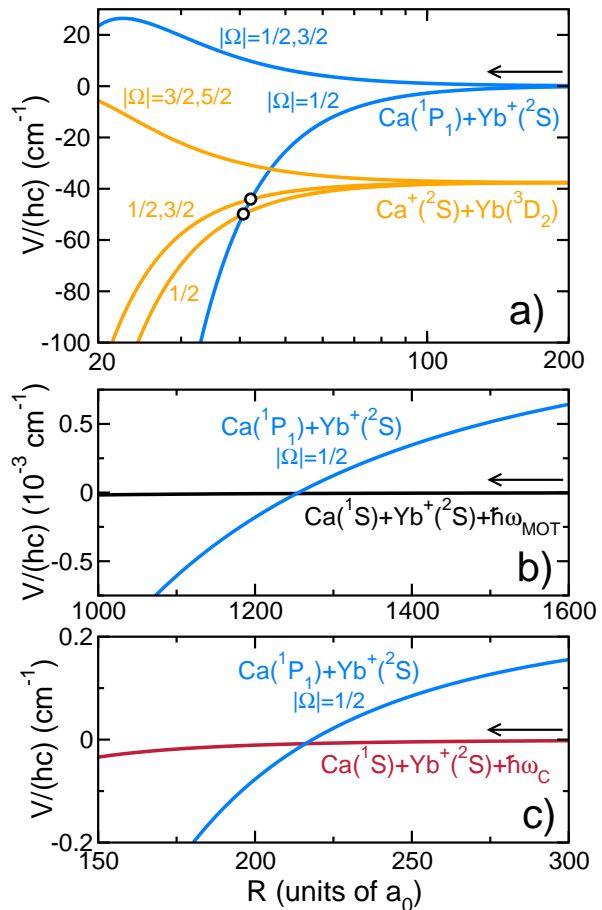
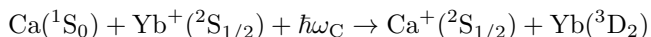


FIG. 1. a) Long-range diabatic potential energy curves in the atomic basis as functions of atom-ion separation  $R$  on a logarithmic scale. Blue and orange curves dissociate to the  $\text{Ca}(4s4p\ ^1P_1)+\text{Yb}^+(6s\ ^2S_{1/2})$  and  $\text{Ca}^+(4s\ ^2S_{1/2})+\text{Yb}(5d6s\ ^3D_2)$  limits, respectively. Curves are labeled by  $|\Omega|$  and the zero of energy is located at the top-most dissociation limit. The two crossings between potentials relevant for charge-transfer are indicated with circular markers. b) Photon-dressed potential energies as functions of  $R$  for pathway II as defined in the text. The black curve is the dressed-state potential dissociating to  $\text{Ca}(4s^2\ ^1S_0)+\text{Yb}^+(6s\ ^2S_{1/2})$  plus one MOT photon. The blue curve is for the attractive potential dissociating to the  $\text{Ca}(4s4p\ ^1P_1)+\text{Yb}^+(6s\ ^2S_{1/2})$  limit. c) Photon-dressed potential energy curves as functions of  $R$  for pathway III. The dark red curve is the dressed-state potential dissociating to  $\text{Ca}(4s^2\ ^1S_0)+\text{Yb}^+(6s\ ^2S_{1/2})$  plus one catalyst photon. The blue curve is as in panel b). Black arrows in panels a), b), and c) indicate the entrance channel for pathway I, II, and III, respectively. The zero of energy in panels b) and c) is located at the dressed ground-state dissociation limit.

is also photon assisted. In this case a tunable catalyst laser with frequency  $\omega_C$  is introduced with the goal to enhance the charge-transfer rate coefficient. The dressed ground-state potential is shown in Fig. 1(c) and crosses the same intermediate potential as in the second pathway. Here, the diabatic crossing and coupling occur at

separation  $R$  of  $200a_0$  to  $500a_0$ . The laser is detuned to the red of the Ca  $1S_0 \rightarrow 1P_1$  transition by tens to hundreds of  $\Gamma$ .

## B. Model ingredients

Conventionally one would compute CT rate coefficients for scattering from the potentials shown in Fig. 1(a), their  $\Omega$ -conserving electronic couplings, as well as  $\Omega$ -changing (and conserving) couplings induced by the relative atom-ion rotational interaction using a coupled-channels (CC) model. For the relevant collision energies  $E = k_B \times 1$  mK to  $k_B \times 10$  K and the long-range  $1/R^3$  charge-quadrupole nature of the potentials, however, contributions to the rate coefficients from a large number of total molecular angular momenta  $\vec{J}$  need to be included. Here,  $k_B$  is the Boltzmann constant and  $\vec{J}$  is the vector sum of the atom-ion total angular momenta and the relative mechanical orbital angular momentum  $\vec{l}$ , which is conserved in the absence of radiation.

To keep the computational effort tractable we employ the infinite-order sudden approximation (IOSA) [25–28], in which Coriolis couplings between different  $\Omega$  states are neglected and, for a given  $J$ , uses a centrifugal potential  $\hbar^2[\mathcal{L}(\mathcal{L} + 1)]/(2\mu R^2)$  for each diagonal matrix element of the potential matrix. Here the integer-valued  $\mathcal{L}$  is an “average” orbital angular momentum quantum number and  $\mu$  is the reduced mass. We choose  $\mathcal{L} = J - 1/2$  justified by the observation that for our entrance channels the sum of the atom-ion total angular momenta is  $1/2$  (in units of  $\hbar$ ). The resulting potential matrix is block diagonal in  $\Omega$ ,  $J$ , and the projection  $M$  of  $\vec{J}$  along the space-fixed laboratory axis. In fact, the matrix and thus rate coefficients are independent of  $M$ . Consequently, we only need to solve for a small set of coupled Schrödinger or coupled-channels (CC) equations for each  $J$  with  $M = 0$  and  $\Omega = 1/2$  using standard methods [29].

Moreover, collisions on the four degenerate repulsive  $|\Omega| = 1/2$  and  $3/2$  Ca( $4s4p\ 1P_1$ ) + Yb $^+(6s\ 2S_{1/2})$  potentials will not lead to significant charge-transfer as the reactants for our small relative collision energies are unlikely to tunnel through the  $\approx hc \times 20\text{ cm}^{-1}$  barrier of these repulsive potentials. Nevertheless, these potentials will play an important role in the rate coefficient as population in the corresponding states is inevitable.

## C. Diabatic coupling

Coupling between the diabatic channels is a second ingredient in setting up our CC model. Its strength is most important where potentials cross. Figure 1 shows three such points, but only two, located at  $R_c = 40.7a_0$  and  $42.3a_0$ , respectively, lead to charge-transfer. Their coupling, in the diabatic basis which stipulates that the electronic wavefunctions barely change with  $R$ , comes from

the overlap between the wavefunctions of the transferring electron on either the Ca nucleus or the Yb nucleus. Such interaction is Coulombic in nature and conserves the body-fixed projection  $\Omega$ . Hence, only crossings between  $|\Omega| = 1/2$  potentials are relevant. The equivalent model in the adiabatic picture would include an avoided crossing between BO potentials and a non-adiabatic coupling between them that mostly comes from the  $d/dR$  term in the Hamiltonian acting on the overlapping adiabatic electronic wavefunctions.

We construct a diabatic two-channel model [21] near each  $|\Omega| = 1/2$  crossing. Since the two diabatic basis functions have different electronic character, the corresponding non-adiabatic coupling in the adiabatic picture is localized and well approximated by a Lorentzian centered at the crossing point [30]. After transforming into the diabatic picture, we can write  $V_{12}(R) = [V_{11}(R) - V_{22}(R)] \tan[2\vartheta(R)]/2$ , where  $V_{11}(R)$  and  $V_{22}(R)$  are the two diabatic potentials and mixing angle  $\vartheta(R) = \arctan[(R_c - R)/R_0]/2 + \pi/4$  with crossing location  $R_c$  and coupling width  $R_0$ . (With these definitions  $V_{12}(R_c) \propto R_0$ .) The coupling width  $R_0$  is taken to be the same for our two crossings and will be adjusted to lead to theoretical rate coefficients that agree with experimental values in cases where only the first two pathways are involved. The resulting coupling width is used later for all three pathways.

## D. Laser-induced coupling

The MOT and catalyst lasers couple the initial photon-dressed Ca( $4s^2\ 1S_0$ ) + Yb $^+(6s\ 2S_{1/2}) + \hbar\omega_{\text{MOT,C}}$  and excited Ca( $4s4p\ 1P_1$ ) + Yb $^+(6s\ 2S_{1/2})$  channels. Using a dressed-state approach [31] and in the IOSA we find coupling matrix element  $-(1/\sqrt{3})d\sqrt{I/(2c\epsilon_0)}$  in SI units between the initial  $\Omega = \pm 1/2$  channel and the attractive  $\Omega = \pm 1/2$  excited channel with the same  $J$ . Here,  $I$  is the MOT or catalyst laser intensity,  $\epsilon_0$  is the electric constant, dipole moment  $d = \sqrt{S/3} = 2.85ea_0$ , using line strength  $S$  of the  $4s^2\ 1S_0$  to  $4s4p\ 1P_1$  transition of Ca [32], and  $e$  is the electron charge. The factor  $1/\sqrt{3}$  accounts for the polarization of the laser projected onto the body-fixed coordinate frame. Direct laser-induced couplings between the ground  $\Omega = \pm 1/2$  and the attractive excited  $\mp 1/2$  channels do not occur. This is because in the body-fixed frame, the attractive excited channels has  $\Omega_{\text{Ca}} = 0$  and the transition preserves the projection quantum number of Yb due to the fact that the transition dipole moment in the long-range (where the transition most likely to happen) originates from the excitation of outer electrons of the Ca atom. The lasers also couple the ground-state channel to repulsive excited  $|\Omega| = 1/2$  and  $3/2$  channels. The repulsive channels, however, do not significantly contribute to the charge-transfer process and their laser-induced coupling matrix elements are not required.

Laser-induced couplings persist to  $R \rightarrow \infty$  and for

pathways II and III we must diagonalize the asymptotic potential matrix and use its eigenvectors and the average partial wave quantum number  $\mathcal{L}$  to define a dressed scattering basis. For pathway I, where light does not dress states, the original atomic basis states can be used. For each of the three pathways we can then solve the coupled-channels equation for  $|\Omega| = 1/2$  and each  $\mathcal{L}$  (or equivalently  $J$ ) and compute the charge-transfer cross section  $\sigma_i(E, \mathcal{L})$  for  $i=I, II, III$  and relative kinetic energy  $E$  of the corresponding initial state. The multiplicity factor of  $(2\mathcal{L} + 1)$  is included in obtaining the cross section.

### E. Spontaneous decay

Charge-transfer involving the excited  $\text{Ca}(4s4p^1P_1)$  state is affected by spontaneous emission [33–35], which limits the probability of colliding particles to remain in the excited channel and reach the diabatic crossing region near  $R \approx 40a_0$ , where CT is most likely to occur. For our first pathway,  $\text{Ca}(4s4p^1P_1)$  and  $\text{Yb}^+(6s^2S_{1/2})$  start at very large  $R$ . For the second and third pathways the excitation to the intermediate  $\text{Ca}(4s4p^1P_1) + \text{Yb}^+(6s^2S_{1/2})$  state is resonant at separations where the energy of the  $|\Omega| = 1/2$  ground-state potential plus the energy of a laser photon equals the attractive  $|\Omega| = 1/2$  of the intermediate channel as shown in Figs. 1(b) and (c). This occurs at  $R \approx 1200a_0$  for pathway II and between  $200a_0$  and  $500a_0$  for pathway III depending on detuning. The classical time for the atom and ion to be pulled together to separations near  $R_c$  by the attractive excited potentials at ultra-cold collision energies can approach or exceed the  $\tau = 4.59$  ns  $\text{Ca}(4s4p^1P_1)$  lifetime.

We account for this spontaneous decay by computing the survival probability  $p_i(E, \mathcal{L})$  to reach crossing points  $R_c$  for initial collision energy  $E$  and average partial wave  $\mathcal{L}$  for each pathway  $i$  [36]. In essence, the probability is based on computing the collision time along classical trajectories on the attractive excited  $\text{Ca}(4s4p^1P_1) + \text{Yb}^+(6s^2S_{1/2})$   $|\Omega| = 1/2$  potential. More details are given in Appendix A. The cross section obtained from the CC calculation and the survival probability are combined to define total CT rate coefficient

$$k_i(E) = f_i \sum_{\mathcal{L}=0}^{\infty} p_i(E, \mathcal{L}) v_{\text{rel}} \sigma_i(E, \mathcal{L}) \quad (1)$$

for  $i=I, II, III$ , where  $v_{\text{rel}} = \sqrt{2E/\mu}$  is the absolute value of the relative velocity  $\vec{v}_{\text{rel}}$ . The factor  $f_i = \eta/3$ ,  $1-\eta$ , and  $1-\eta$  for  $i=I, II, III$ , respectively. For pathway I it accounts for the fact that in a MOT a fraction  $\eta$  of the Ca atoms is in the excited state and that only the two (degenerate) attractive  $|\Omega| = 1/2$   $\text{Ca}(4s4p^1P_1) + \text{Yb}^+(6s^2S_{1/2})$  channels out of the six excited states lead to charge-transfer. For pathway II and III  $f_i$  is simply the fraction of Ca atoms in the ground state as both initial states,  $\Omega = \pm 1/2$ , equally contribute to the CT rate coefficient. We use the MOT parameter in Ref. [37], which

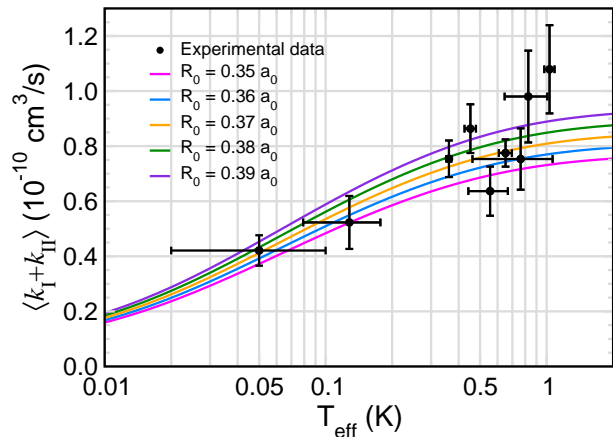


FIG. 2. Total thermalized charge-transfer rate coefficient in a Ca MOT as a function of effective temperature  $T_{\text{eff}}$  in the center-of-mass frame. Filled black circles with one-standard deviation error bars are our experimental data points. Solid lines are theoretical predictions with coupling width  $R_0$  ranging from  $0.35a_0$  to  $0.39a_0$ . The MOT laser has an intensity of  $78 \text{ mW/cm}^2$  and is red detuned from the  $\text{Ca } ^1S_0$  to  $^1P_1$  transition by one natural linewidth, such that 9.2% of the Ca atoms are in the  $^1P_1$  state.

leads to  $\eta = 0.092$ , in our calculations. As the ion temperature  $T_i$  is much larger than that of the atoms, the relative velocity distribution in the center-of-mass frame can be described by the three-dimensional Gaussian probability distribution  $P(\vec{v}_{\text{rel}}) \propto \exp(-\mu v_{\text{rel}}^2/[2k_B T_{\text{eff}}])$  with effective temperature  $T_{\text{eff}} = m_{\text{Ca}} T_i / M$ ,  $M = m_{\text{Ca}} + m_{\text{Yb}}$ , and Ca and  $\text{Yb}^+$  masses  $m_{\text{Ca}}$  and  $m_{\text{Yb}}$ , respectively. We use this distribution to thermally average the charge-transfer rate coefficient.

## III. RESULTS

### A. Pathway I and II: MOT-induced charge-transfer

Figure 2 compares our total charge-transfer rate coefficients as measured in the MOT with the thermalized theoretical  $\langle k_I(E) + k_{II}(E) \rangle$  for several values of  $R_0$  as a function of effective temperature  $T_{\text{eff}}$  between 0.01 K and 2 K. The data shows a significant decrease of the rate coefficient due to the suppression from spontaneous decays as the temperature lowers by over an order of magnitude. Additional analysis shows that about 40% of the theoretical rate coefficient is due to the first pathway. The figure also shows that at a fixed temperature the rate coefficient increases monotonically when the coupling width  $R_0$  increases from  $0.35a_0$  to  $0.39a_0$ . The theoretical values agree well with the experimental data. The coupling strength  $V_{12}(R = R_c)$  for these  $R_0$  at the crossing points is approximately  $hc \times 0.5 \text{ cm}^{-1}$ . In further support of the theoretical model and the resulting value of  $R_0$ , we obtained comparable coupling strength at  $R_c$

with a Heitler-London type of estimate [38], discussed in detail in Appendix A, using the overlap integral of atomic orbitals and the electron-nuclei Coulomb potential.

### B. Pathway III: Photoassociation-enhanced charge-transfer

In the experiment described in Ref. [37] the addition of a tunable laser with intensity  $I_C$  and (angular) frequency  $\omega_C$  enhances the charge-transfer processes as the third pathway is added. This laser is detuned to the red of the Ca  $^1S_0$  to  $^1P_1$  transition by tens to hundreds of natural linewidths. In fact, the laser excites rovibrational levels of the attractive  $|\Omega| = 1/2$  Ca( $4s^2\ ^1P_1$ )+Yb $^+$ ( $6s\ ^2S_{1/2}$ ) potential. Since the MOT cooling lasers in the experiment are always on, the third pathway coexists with the other two.

In this paper we want to highlight and focus on the effect of the catalyst laser. The relevant diabatic potentials are shown in Figs. 1(a) and (c). The potential matrix is diagonalized asymptotically to form the correct scattering basis. By solving the CC equations, we obtain the partial cross sections for the third pathway,  $\sigma_{\text{III}}(E, \mathcal{L}, \omega_{\text{pa}})$ . The survival probability  $p_{\text{III}}(E, \mathcal{L}, \omega_C)$  is larger than for the second pathway. This is because the crossing between the dressed entrance channel and the intermediate excited channel occurs at  $R \sim 200 - 500 a_0$ , depending on  $\omega_C$ , which is much smaller than for the second pathway. Thus, the reactants are quickly accelerated along the excited attractive  $1/R^3$  potential and need much less time to reach  $R_c$  to react.

The addition of pathway III via the catalyst laser enhances the charge-transfer reaction by adding  $k_{\text{III}}(E)$  to the total rate coefficient  $k_{\text{tot}}(E)$ , while leaving  $k_{\text{I}}(E)$  and  $k_{\text{II}}(E)$  unchanged to good approximation. Figure 3 shows an example of  $k_{\text{III}}(E)$  as a function of the laser detuning at collision energy  $E = k_B \times 1$  mK. It is evident that the charge-transfer reaction occurs in a resonant fashion with a larger number of narrow peaks. The resonance locations cluster and correspond to rotational progressions of the vibrational series of the attractive  $|\Omega| = 1/2$  potential dissociating to the Ca( $4s4p\ ^1P_1$ )+Yb $^+$ ( $6s\ ^2S_{1/2}$ ) threshold. The height of the resonant features decrease with increasing (negative) detuning as the overlap of resonances decrease due to increasing ro-vibrational spacing in the excited potential.

Scattering from thirteen partial waves  $\mathcal{L}$  contribute significantly to the charge-transfer as the 1 mK collision energy roughly corresponds to the height of the centrifugal barrier for the  $\mathcal{L} = 12$  channel. To illustrate this, we compare the locations of the resonances with the rovibrational bound states of the attractive *diabatic* potential dissociating to the Ca( $4s4p\ ^1P_1$ )+Yb $^+$ ( $6s\ ^2S_{1/2}$ ) threshold in Fig. 3. The figure also shows the expected value of  $\mathcal{L}$  for each resonance. In Fig. 3(a), the locations of the onset of each group of resonances closely follow the binding energies of ro-vibrational series.

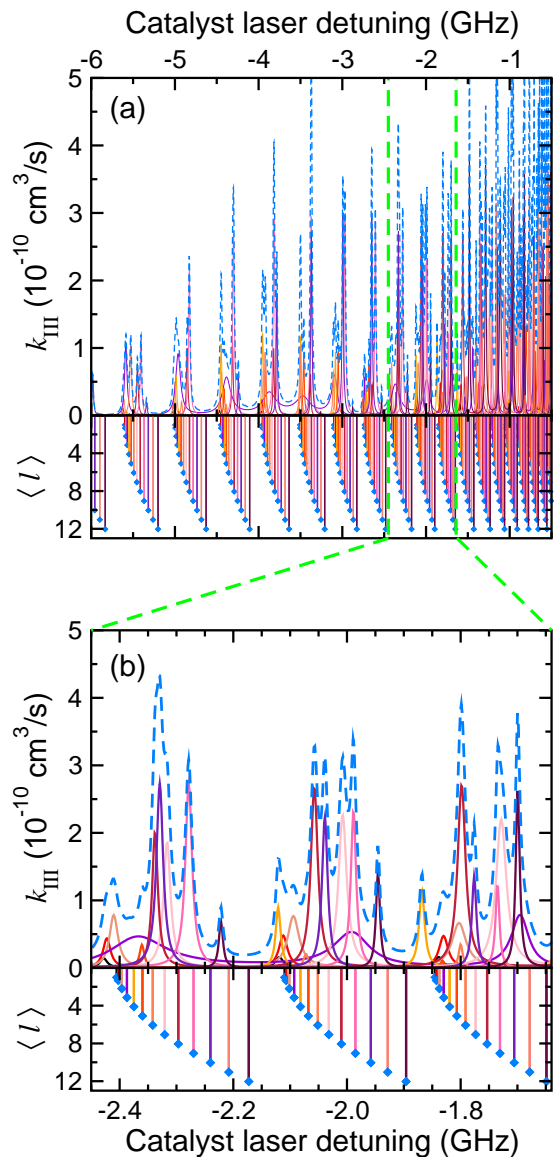


FIG. 3. Charge-transfer rate coefficients from the catalyst laser and assignment of catalyst resonances as functions of the detuning from the Ca  $^1S_0$  to  $^1P_1$  transition for collision energy  $E = k_B \times 1$  mK, laser intensity of  $I_C = 5$  W/cm $^2$ , and coupling width  $R_0 = 0.37a_0$ . The upper panel of subfigure a) shows rate coefficients for detunings between  $-6$  GHz and  $-0.5$  GHz, while the upper panel of subfigure b) shows a blowup near  $-2$  GHz in order to better distinguish the different curves. The dashed blue line corresponds to the total rate coefficient from pathway III, while the various colored solid lines represent contributions from average partial-wave channels  $\mathcal{L} = 0$  to  $12$ . The lower panel in each subfigure shows the rovibrational  $\Omega = 1/2$  bound states dissociating to the Ca( $4s4p\ ^1P_1$ )+Yb $^+$ ( $6s\ ^2S_{1/2}$ ) threshold. The lowest thirteen rotational states for each vibrational state are shown and the colors of the drop lines mimic the colors of the  $\mathcal{L}$  contributions in the upper panels. The  $y$ -axis of the lower panels is the expectation value of  $\mathcal{L}$  of the bound states.

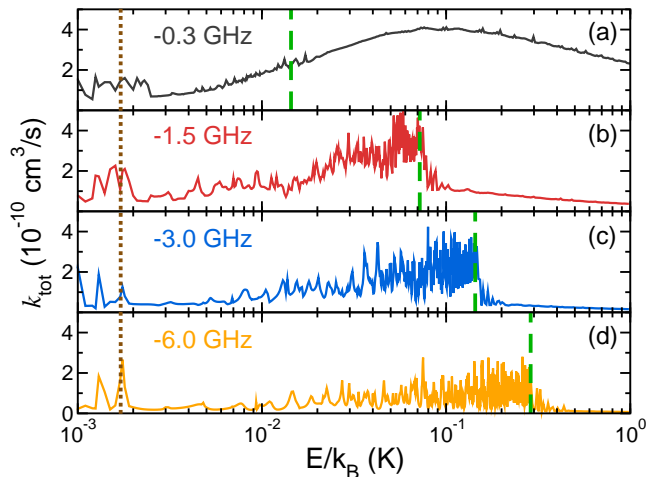


FIG. 4. Total charge-transfer rate coefficients in the presence of the catalyst laser as functions of collision energy  $E$ . In panels a), b), c), and d) the photo-association laser is detuned 0.3 GHz, 1.5 GHz, 3.0 GHz, and 6.0 GHz to the red of Ca  $^1S_0$  to  $^1P_1$  transition, respectively. In each panel the vertical dashed green line represents a collision energy equal to the energy-equivalent of the detuning of the catalyst laser. The vertical dotted brown line is located at  $E = h\Gamma = k_B \times 1.7$  mK, both the energy equivalent of the MOT laser detuning and the natural linewidth of the Ca  $^1P_1$  state. We assume catalyst laser intensity  $I_C = 6$  W/cm $^2$  and coupling width  $R_0 = 0.39a_0$ .

Figure 3(b) shows a blowup of the spectrum for three vibrational levels in Fig. 3(a). We see that the location of rotational states  $\mathcal{L}$  does not directly follow the location of the corresponding resonances. The shifts are due to interferences with the charge-transferred  $\text{Ca}^+(^2S) + \text{Yb}(^3D_2)$  exit channels induced by the non-perturbative short-range couplings.

Figure 4 shows an example total charge-transfer rate coefficient  $k_{\text{tot}}(E)$  as a function of collision energy at four detunings,  $\delta$ , of the catalyst laser. The laser intensity is two orders of magnitude larger than  $I_{\text{MOT}}$ . For  $\delta = -0.3$  GHz,  $k_{\text{tot}}(E)$  has a smooth behavior, interlaced with weak narrow features, and a maximum near  $E = k_B \times 0.1$  K. For larger detunings sharp features dominate, while above a critical collision energy the rate coefficient rapidly approaches zero. For all detunings strong resonances are visible for  $E < k_B \times 2$  mK.

The behavior for large catalyst laser detunings can be understood from comparison of the collision energy with  $h\delta$ , the dashed green lines in Fig. 4. For  $E < h\delta$  pathway III contributes resonances to the total rate coefficient due to the coupling between the entrance channel continuum and the bound states of the attractive intermediate  $|\Omega| = 1/2$  potential. When the collision energy exceeds  $h\delta$ , the entrance continuum is only coupled to scattering states of the intermediate channel. Their coupling matrix elements are much smaller than those between

continuum-bound states and the rate coefficient becomes much smaller.

For  $\delta = -0.3$  GHz, the total rate coefficient does not turn off at  $h\delta$  thanks to pathway III as a consequence of the fact that for small detunings the energy spacing between excitable vibrational levels is smaller and resonances begin to overlap. In fact, helped by the relatively high-powered catalyst laser, interference between the broadened resonances becomes important. Hence, the resonances behave almost like a continuum and the rate coefficient is a smooth function of  $E$  both for energies smaller and larger than  $h\delta$ . The same effect is not obvious for the MOT laser pathway due to the much smaller laser intensity that couples the continuum and the bound states much weakly and does not broaden the resonances nearly as much despite the smaller detuning.

Finally, pathway II contributes resonances to the total rate coefficient for collision energies comparable or smaller than  $k_B \times 2$  mK, roughly corresponding to the detuning of the MOT laser  $h\Gamma = k_B \times 1.7$  mK labeled by the brown dashed-lines. These resonances correspond to bound states with extremely-long-range outer turning points in the intermediate  $|\Omega| = 1/2$  potential.

#### IV. CONCLUSION

In conclusion, we have presented experimental measurements and results from a close-coupling model of photon-induced charge-transfer in  $\text{Ca} + \text{Yb}^+$  that yielded insight into three contributing reaction mechanisms. The model relies on a dense manifold of electronically-excited long-range induction and dipolar potentials, their non-adiabatic coupling, and survival probabilities against spontaneous emission of the excited Ca atom. It leads to a high charge-transfer rate coefficient of the order of  $10^{-11} - 10^{-10}$  cm $^3$ /s in agreement with the experimental results [37].

#### V. ACKNOWLEDGMENTS

Work at the Temple University is supported by the MURI Army Research Office Grant No. W911NF-14-1-0378 and Grant No. W911NF-17-1-0563, the U.S. Air Force Office of Scientific Research Grant No. FA9550-14-1-0321 and the NSF Grant No. PHY-1619788. Work at UCLA is supported in part by National Science Foundation (PHY-1255526, PHY-1415560, and DGE-1650604) and Army Research Office (W911NF-15-1-0121, W911NF-14-1-0378, and W911NF-13-1-0213) grants.

#### Appendix A: Long-range interaction potentials

We now describe in more detail the long-range diabatic interaction potentials between excited Ca and  $\text{Yb}^+$  coupled to  $\text{Ca}^+$  and excited Yb as shown in Fig. 1(a). The

interaction between an excited atom and an ion has two contributions. The first arises from the interaction between the ion charge and the quadrupole moment of the excited atom and has an anisotropic  $C_3/R^3$  dependence on atom-ion separation  $\vec{R}$ , where  $C_3$  depends on the orientation of  $\vec{R}$ . The second term is an anisotropic  $C_4/R^4$  interaction, where  $C_4$  also depends on the orientation of  $\vec{R}$ . It originates in second-order perturbation theory from the interaction between the charge and the induced dipole moment of the neutral atom. Consequently, both  $C_3$  and  $C_4$  only depend on the properties of the neutral atom.

Our diabatic potentials are the diagonal matrix elements of the molecular interaction in the atomic basis in the body-fixed frame  $|q_a j_a \Omega_a, q_b j_b \Omega_b\rangle = |q_a, j_a \Omega_a\rangle |q_b, j_b \Omega_b\rangle$  labeled by charge state  $q_s = 0, +1$  and body-fixed projection quantum number  $\Omega_s$  of the angular momentum  $j_s$  of the atom or ion along the internuclear axis, where  $s = a$  and  $b$  for Ca and Yb, respectively. This uniquely labels the atomic states relevant for our system. Electronic molecular interactions always conserve  $\Omega = \Omega_a + \Omega_b$ .

Crucially, for our system both contributions to the long-range potential are diagonal in this body-fixed basis [31]. The matrix elements of  $C_3$ , expressed in two equivalent ways, are

$$C_{3, j_s \Omega_s} = q \frac{\langle j_s \Omega_s | j_s 2 \Omega_s 0 \rangle Q}{\langle j_s j_s | j_s 2 j_s 0 \rangle 2} \\ = q (-1)^{j_s - \Omega_s} \begin{pmatrix} j_s & 2 & j_s \\ -\Omega_s & 0 & \Omega_s \end{pmatrix} \langle j_s || Q_2 || j_s \rangle,$$

where the quantum numbers  $j_s \Omega_s$  always describe the state of the neutral atom,  $q = +1$  for the corresponding ion,  $(:::)$  denotes a Wigner 3- $j$  symbol, and  $\langle j_1 m_1 | j_2 j_3 m_2 m_3 \rangle$  is a Clebsch-Gordan coefficient. Finally,  $Q$  is the quadrupole moment defined in Refs. [39, 40], while  $\langle j_s || Q_2 || j_s \rangle$  is the reduced matrix element used by Refs. [40, 41]. For  $^1P_1$  Ca state the quadrupole moment is positive with  $|Q| = 11.04 e a_0^2$  [39]. The sign convention is derived from Ref. [42]. For the  $^3D_2$  state of Yb,  $\langle j_s || Q_2 || j_s \rangle = +14.2 e a_0^2$  [41].

The diagonal matrix elements of the  $C_4$  coefficient are [43]

$$C_{4, j_s \Omega_s} = -\frac{q^2}{2} \left[ \alpha_{0, j_s} + \alpha_{2, j_s} \frac{3\Omega_s^2 - j_s(j_s + 1)}{j_s(2j_s - 1)} \right],$$

where  $\alpha_{0, j_s}$  is the static scalar polarizability and  $\alpha_{2, j_s}$  is the static tensor polarizability of the neutral atom in state  $|0, j_s \Omega_s\rangle$ . For the Ca  $^1P_1$  state,  $\alpha_{0,1} = 242.4 a_0^3$  and  $\alpha_{2,1} = -55.3 a_0^3$  [39]. For the Yb  $^3D_2$  state,  $\alpha_{0,2} = 61 a_0^3$  and  $\alpha_{2,2} = 28 a_0^3$  [41, 44].

Finally, the long-range interaction between a neutral S-state atom and a S-state ion has an isotropic, attractive  $C_4/R^4$  dependence on  $R$ . For Ca+Yb $^+$  it is shown in Figs.1(b) and (c) as the dressed state potential. The  $C_4$  coefficient equals  $-\alpha_{0,0}/2$ , where  $\alpha_{0,0}$  is the static

TABLE I. The  $C_3$  and  $C_4$  coefficients of the attractive long-range  $\Omega = 1/2$  diabatic potentials in atomic units and quantum numbers for the corresponding Ca+Yb $^+$  or Ca $^+$ +Yb channels. Channels are uniquely described by the charge  $q_i$ , atomic angular momenta  $j_i$ , and its body-fixed projection  $\Omega_i$  on the internuclear axis with  $i = a$  and  $b$  for Ca and Yb, respectively. Potentials are degenerate for  $-\Omega$  and  $\Omega$ , where  $\Omega = \Omega_a + \Omega_b$ .

Ca/Ca $^+$			Yb/Yb $^+$			$C_3$	$C_4$
$q_a$	$j_a$	$\Omega_a$	$q_b$	$j_b$	$\Omega_b$		
0	0	0	+1	1/2	1/2	0	-78.55
0	1	0	+1	1/2	1/2	-11.04	-176.74
+1	1/2	1/2	0	2	0	-3.39	-16.5
+1	1/2	-1/2	0	2	1	-1.70	-23.5

polarizability of the neutral atom. The  $C_3$  coefficient is zero as S-state atoms have zero quadrupole moment.

Table I gives the relevant  $C_3$  and  $C_4$  coefficients as well as lists the quantum numbers of the channels. A negative sign indicates attractive interactions. At smaller separations (not shown in Fig. 1) each potential transitions to a repulsive  $C_{12}/R^{12}$  potential.

Diabatic potentials with the same  $\Omega$  cross and couple near  $R_c \approx 40 a_0$ . As discussed in the main text, we have opted to use model coupling function with coupling width  $R_0$ . The value of  $R_0$  is fitted to experimental data and estimated to be between 0.35 and 0.39  $a_0$ . In support of our model and fitting result, we can also estimate the diabatic coupling strength at  $R = R_c$  based on a Heitler-London method. In atomic units, we can write the coupling matrix element between the attractive  $|\Omega| = 1/2$  Ca( $4s4p \ ^1P_1$ )+ Yb( $6s \ ^2S_{1/2}$ ) and Ca $^+$ ( $4s \ ^2S_{1/2}$ )+Yb( $5d6s \ ^3D_2$ ) channels as

$$V_{12}(R) \sim \langle \text{Ca}(4p) | \frac{1}{r_{\text{Ca}}} + \frac{1}{r_{\text{Yb}}} | \text{Yb}(5d) \rangle, \quad (\text{A1})$$

where  $|\text{Ca}(4p)\rangle$  and  $|\text{Yb}(5d)\rangle$  are the Ca  $4p$  and Yb  $5d$  Hartree-Fock electronic orbitals, respectively, and the electron coordinate for the two orbitals is  $\vec{r}_{\text{Ca}, \text{Yb}}$  with respect to the Ca and Yb nuclei, respectively. At  $R = R_c$  we find that  $V_{12}(R_c)$  is on the order of  $hc \times 0.5 \text{ cm}^{-1}$  which corresponds to the range of  $R_0$  we obtained.

## Appendix B: Survival probabilities

The evaluation of survival probabilities within the IOSA framework on the attractive excited potential  $V_e(R)$  of the  $|\Omega| = 1/2$  Ca( $4s^2 \ ^1P_1$ )+Yb $^+$ ( $6s \ ^2S_{1/2}$ ) channel due to spontaneous decay of the Ca  $^1P_1$  state can be treated with rate equations for populations derived from the optical Bloch equations [36, 45]. Here, the atom pair decays back to the ground-state potential  $V_g(R)$  of the  $|\Omega| = 1/2$  Ca( $4s^2 \ ^1S_0$ )+Yb $^+$ ( $6s \ ^2S_{1/2}$ ) channel. In a MOT we can assume that the coherence between the Ca  $^1S_0$  and  $^1P_1$  states decays much faster

than those of the populations. Moreover, at our temperatures where a large number of relative orbital angular momenta  $\mathcal{L}$  contribute, the relative nuclear motion for the purpose of estimating the survival probability can be described by classical evolution  $R(t)$  on the potential  $U_e(R; \mathcal{L}) = V_e(R) + \hbar^2 \mathcal{L}(\mathcal{L} + 1)/(2\mu R^2)$  from the excitation region at (very) large separation at  $t = 0$  to  $R_c \approx 40a_0$ , the separation where charge-transfer occurs. At  $t = 0$  the atom pair has relative kinetic energy  $E$  and is moving towards smaller  $R$ .

Under these assumption we have for pathway I

$$\frac{dp_e(t)}{dt} = -\Gamma p_e(t) - \Gamma'(t) p_e(t) + \frac{1}{3} \Gamma'(t) p_g(t) \quad (\text{B1})$$

and  $p_g(t) + 3p_e(t) = 1$ , where  $p_g(t)$  and  $p_e(t)$  are the populations in the ground- and excited-state channel, respectively. Here,  $\Gamma$  is the natural linewidth of  $\text{Ca}(^1\text{P}_1)$ , and

$$\Gamma'(t) = A_\Gamma \frac{\gamma^3}{\Delta E(t)^2 + \gamma^2}, \quad (\text{B2})$$

describes the stimulated absorption and emission rate of MOT photons, where  $\gamma = \Gamma/2$  and the time-dependent  $\Delta E(t) = V_e(R(t)) - V_g(R(t)) - \hbar\omega_{\text{MOT}}$  at separation  $R(t)$ . The last term on the right-hand side of Eq. B1 accounts for processes where, after a spontaneous emission event, the atom pair is again excited and participates in the charge-transfer collision. The factor of one third in this term accounts for the fact that only one third of the photons are able to excite the system back to the attractive excited channels.

The constant  $A_\Gamma$  is set such that the steady-state solution of Eq. B1 for  $R \rightarrow \infty$  reproduces the experimental

fraction of atom pairs in the  $|\Omega| = 1/2$  excited potential  $V_e(R)$ , i.e.  $p_e|_{R \rightarrow \infty} = \eta/3$ , where  $\eta$  is the fraction of Ca atoms in the  $^1\text{P}_1$  state. For the MOT parameters in Ref. [37]  $\Delta E \rightarrow -\Gamma$  for  $R \rightarrow \infty$  and  $\eta = 0.092$ .

In practice, we do not solve Eq. B1 directly but rephrase the equation into one for separation  $R$  by noting that  $dt = dR/v(R; E, \mathcal{L})$ , where velocity  $v(R; E, \mathcal{L})$  satisfies  $\mu v^2/2 + U_e(R; \mathcal{L}) = E$  for each  $R$ . The radial differential equation can be integrated from very large  $R$  to crossing point  $R_c$  to obtain survival probability  $p_I(E, \mathcal{L})$  for pathway I.

Our second pathway is also affected by spontaneous decay of the excited channels. In this case the excitation occurs near  $R_x \approx 1200a_0$ . The stimulated excitation and decay are already included in the close-coupling calculations when the light coupling is included and the asymptotic basis functions diagonalized, thus do not need to be included here. We then find the simpler differential equation

$$\frac{dp_e(t)}{dt} = -\Gamma p_e(t), \quad (\text{B3})$$

which is transformed into one for  $R$  and solved from  $R = R_x$  with  $p_e(R_x) = 1$  to  $R_c$  assuming an initial kinetic energy  $E$  and average partial wave  $\mathcal{L}$ . The final value at  $R_c$  defines the survival probability  $p_{II}(E, \mathcal{L})$  for this pathway. The differential equation for the third pathway is the same as for pathway II, but now the excitation separation is even smaller and we find that the  $p_{III}(E, \mathcal{L})$  are larger than 0.1 for the detunings considered here.

- 
- [1] R. Coté and A. Dalgarno, Phys. Rev. A **62**, 012709 (2000).
- [2] A. Watanabe, C. M. Dutta, P. Nordlander, M. Kimura, and A. Dalgarno, Phys. Rev. A **66**, 044701 (2002).
- [3] L. B. Zhao, P. C. Stancil, J. P. Gu, H. Liebermann, Y. Li, P. Funke, R. J. Buenker, B. Zygelman, M. Kimura, and A. Dalgarno, The Astrophysical Journal **615**, 1063 (2004).
- [4] A. T. Grier, M. Cetina, F. Oručević, and V. Vuletić, Phys. Rev. Lett. **102**, 223201 (2009).
- [5] P. Zhang, E. Bodo, and A. Dalgarno, J. Phys. Chem. A **113**, 15085 (2009).
- [6] Z. Idziaszek, T. Calarco, P. S. Julienne, and A. Simoni, Phys. Rev. A **79**, 010702 (2009).
- [7] C. Zipkes, S. Palzer, L. Ratschbacher, C. Sias, and M. Köhl, Phys. Rev. Lett. **105**, 133201 (2010).
- [8] S. Schmid, A. Härter, and J. H. Denschlag, Phys. Rev. Lett. **105**, 133202 (2010).
- [9] F. H. J. Hall, M. Aymar, N. Bouloufa-Maafa, O. Dulieu, and S. Willitsch, Phys. Rev. Lett. **107**, 243202 (2011).
- [10] X. J. Liu, Y. Z. Qu, B. J. Xiao, C. H. Liu, Y. Zhou, J. G. Wang, and R. J. Buenker, Phys. Rev. A **81**, 022717 (2010).
- [11] P. Zhang, A. Dalgarno, R. Cote, and E. Bodo, Phys. Chem. Chem. Phys. **13**, 19026 (2011).
- [12] M. Tacconi, F. A. Gianturco, and A. K. Belyaev, Phys. Chem. Chem. Phys. **13**, 19156 (2011).
- [13] W. G. Rellergert, S. T. Sullivan, S. Kotochigova, A. Petrov, K. Chen, S. J. Schowalter, and E. R. Hudson, Phys. Rev. Lett. **107**, 243201 (2011).
- [14] H. D. L. Lamb, J. F. McCann, B. M. McLaughlin, J. Goold, N. Wells, and I. Lane, Phys. Rev. A **86**, 022716 (2012).
- [15] A. K. Belyaev, S. A. Yakovleva, M. Tacconi, and F. A. Gianturco, Phys. Rev. A **85**, 042716 (2012).
- [16] E. R. Sayfutyarova, A. A. Buchachenko, S. A. Yakovleva, and A. K. Belyaev, Phys. Rev. A **87**, 052717 (2013).
- [17] B. M. McLaughlin, H. D. L. Lamb, I. Lane, and J. F. McCann, J. Phys. B **47**, 145201 (2014).
- [18] S. Haze, R. Saito, M. Fujinaga, and T. Mukaiyama, Phys. Rev. A **91**, 032709 (2015).
- [19] S. T. Sullivan, W. G. Rellergert, S. Kotochigova, and E. R. Hudson, Phys. Rev. Lett. **109**, 223002 (2012).
- [20] P. Puri, M. Mills, C. Schneider, I. Simbotin, J. A. Montgomery, R. Côté, A. G. Suits, and E. R. Hudson, Science **357**, 1370 (2017).



- [21] E. E. Nikitin, in *Springer Handbooks of Atomic, Molecular, and Optical Physics*, edited by G. W. F. Drake (Springer, New York, 2006) Chap. 49, pp. 741–752.
- [22] B. Zygelman, Z. Lucic, and E. R. Hudson, *Journal of Physics B: Atomic, Molecular and Optical Physics* **47**, 015301 (2014).
- [23] M. Tomza, C. P. Koch, and R. Moszynski, *Phys. Rev. A* **91**, 042706 (2015).
- [24] B. Gao, *Phys. Rev. A* **83**, 062712 (2011).
- [25] R. T. Pack, *The Journal of Chemical Physics* **60**, 633 (1974).
- [26] D. Secrest, *The Journal of Chemical Physics* **62**, 710 (1975).
- [27] L. W. Hunter, *The Journal of Chemical Physics* **62**, 2855 (1975).
- [28] D. J. Kouri, in *Atom - Molecule Collision Theory*, edited by R. B. Bernstein (Springer, New York, 1979) pp. 301–358.
- [29] R. G. Gordon, *J. Chem. Phys.* **51**, 14 (1969).
- [30] H. Werner and W. Meyer, *J. Chem. Phys.* **74**, 5802 (1981).
- [31] A. Petrov, C. Makrides, and S. Kotochigova, *J. Chem. Phys.* **146**, 084304 (2017).
- [32] Y. Yu and A. Derevianko, *Atomic Data and Nuclear Data Tables* **119**, 263 (2018).
- [33] A. Gallagher and D. E. Pritchard, *Phys. Rev. Lett.* **63**, 957 (1989).
- [34] P. Julienne, A. Smith, and K. Burnett, in *Advances In Atomic, Molecular, and Optical Physics*, edited by D. Bates and B. Bederson (Academic Press, 1992) Chap. 30, pp. 141 – 198.
- [35] H. M. J. M. Boesten, B. J. Verhaar, and E. Tiesinga, *Phys. Rev. A* **48**, 1428 (1993).
- [36] K.-A. Suominen, M. J. Holland, K. Burnett, and P. S. Julienne, *Phys. Rev. A* **49**, 3897 (1994).
- [37] M. Mills, P. Puri, M. Li, S. J. Schowalter, A. Dunning, C. Schneider, S. Kotochigova, and E. R. Hudson, to be published (2018).
- [38] K. Tang, J. P. Toennies, and C. L. Yiu, *International Reviews in Physical Chemistry* **17**, 363 (1998).
- [39] J. Mitroy and J.-Y. Zhang, *J. Chem. Phys.* **128**, 134305 (2008).
- [40] A. Derevianko, *Phys. Rev. Lett.* **87**, 023002 (2001).
- [41] Buchachenko, A. A., *Eur. Phys. J. D* **61**, 291 (2011).
- [42] S. C. Ceraulo and R. S. Berry, *Phys. Rev. A* **44**, 4145 (1991).
- [43] J. Mitroy, M. S. Safronova, and C. W. Clark, *Journal of Physics B: Atomic, Molecular and Optical Physics* **43**, 202001 (2010).
- [44] C. J. Bowers, D. Budker, S. J. Freedman, G. Gwinner, J. E. Stalnaker, and D. DeMille, *Phys. Rev. A* **59**, 3513 (1999).
- [45] C. Cohen-Tannoudji, J. Dupont-Roc, and G. Grynberg, “Optical Bloch equations,” in *Atom-Photon Interactions* (Wiley-Blackwell, 2008) Chap. 5, pp. 353–405.